Journal of Zhejiang University-SCIENCE A (Applied Physics & Engineering)
ISSN 1673-565X (Print); ISSN 1862-1775 (Online)
www.jzus.zju.edu.cn; www.springerlink.com
E-mail: jzus@zju.edu.cn

Deformational characteristics of sensor-enabled geobelts incorporating two failure modes in reinforced sand*

Yi-lin WANG[1], Xin-zhuang CUI[†‡1], Kai-wen LIU[2]

[1]*School of Civil Engineering, Shandong University, Jinan 250061, China*

[2]*Key Laboratory of High-speed Railway Engineering of Ministry of Education, Southwest Jiaotong University, Chengdu 610031, China*

[†]E-mail: cuixz@sdu.edu.cn

Received Feb. 12, 2020; Revision accepted June 3, 2020; Crosschecked Nov. 16, 2020

Abstract: Geobelt deformation is of significance when making prejudgments on potential failure planes in reinforced structures. A failure plane results from two geobelt failure modes, tensile failure and pullout. In order to investigate the deformation characteristics of geobelts in two failure modes, results from pullout tests on sensor-enabled geobelts (SEGBs) with various lengths in sand are reported here across a range of normal pressures. Self-measurements of SEGB can provide data during the tests regarding distributions of strain, stress, and displacement. Data collected during pullout tests reveal the effects of normal pressures and specimen lengths on failure mode. A critical line considering normal pressure and specimen length is derived to describe the transition between two failure modes, an approach which can be utilized for preliminary predictions of failure mode in pullout tests. Warning criteria established based on critical line and data from the self-measurements of SEGB are proposed for failure mode prediction which can contribute to prejudgments of potential failure plane in geosynthetically reinforced soil structures.

Key words: Geosynthetic; Sensor-enabled geobelt (SEGB); Failure mode; Deformation characteristics; Pullout tests
https://doi.org/10.1631/jzus.A2000056 **CLC number:** TU41

1 Introduction

Geosynthetic reinforcement has a track-record of excellent performance in terms of increasing both stability and stabilizing earth structures as well as improving serviceability by reducing settlement and lateral displacements (Chaiyaput et al., 2014; Xu and Chai, 2014; Rowe and Liu, 2015; Liu, 2016; Yang et al., 2016; Yu et al., 2016; Zhou et al., 2016; King et al., 2017a, 2017b, 2018; Liu et al., 2017, 2018; Mousavi et al., 2017; Ni et al., 2017; Yarivand et al., 2017; Yu and Bathurst, 2017; Luo and Bathurst, 2018). Thus, geosynthetic-reinforced soil structures have been used in projects that are highly sensitive due to their potential impact on public safety and sensitivity including high retaining walls along heavily used traffic arteries (Xiao et al., 2016), in subgrades of high-speed railways (Chen et al., 2016), and in reinforced dam slopes where failure could lead to significant loss of life (Mehrjardi et al., 2016). The potential impacts on human safety and the substantial economic effects of failure of a high-profile reinforced soil structure highlight the need for a means of monitoring their performance over whole lifespans. It is especially important to be able to identify warnings of potential failure or highly degraded performance well enough in advance that maintenance or, if needed, more significant stabilization measures can be initiated to prevent failure.

‡ Corresponding author

* Project supported by the National Key Research and Development Program of China (No. 2018YFB1600100) and the National Natural Science Foundation of China (Nos. 51778346 and 51608461)

ORCID: Yi-lin WANG, https://orcid.org/0000-0003-2212-5747; Xin-zhuang CUI, https://orcid.org/0000-0003-1501-3931

Well-established techniques for monitoring pore pressure, settlement, and lateral movements are useful for monitoring some potential failure modes. However, the analysis of potential failure modes and effects of such structures is also able to quickly identify failure modes that will not be easily predicted. One measure of particular note is degradation in resistance afforded by reinforcement in terms of its anchorage (or its stiffness or strength) relative to demands (loads). These reinforcement characteristics gradually degrade and, generally, will not be evident from traditional monitoring in early deformation stages. Understanding this has prompted the search for an effective method to assess how the effectiveness of geosynthetics inside soil structure changes with time, vital to our understanding of internal damage evolution. Numerical models can be used to simulate the distribution of deformations and forces along geosynthetics inside the soil. In one study, Gurung (2001) used a 1D nonlinear equation to conduct parametric numerical analysis of a pullout test to assess the distributions of tension and displacement along a geobelt (as defined more fully in Section 2.1). Similarly, others researchers (Tran et al., 2013; Pinho-Lopes et al., 2015; Shi et al., 2016; Wang et al., 2016) have used numerical analyses to evaluate pullout tests on various geosynthetics. Numerical analyses have considerable utility for understanding how the performance of a structure might degrade in concert with reinforcement properties. At the same time, these analyses provide limited information on how a real structure actually performs over time. Additional forms of monitoring are needed.

A range of measurement methods are currently available for obtaining in-soil deformations of geosynthetics. In one approach, Allen and Bathurst (2014) investigated the performance of an 11-m high block-faced geogrid wall and measured the strains with gauges and extensometers, while Chen et al. (2016) reported a full-scale experiment study on a geogrid reinforced pile-supported embankment. In this analysis, fiber Bragg grating (FBG) sensors were deployed along geogrid ribs to measure their strains. In another analysis, Mosallanezhad et al. (2016) pulled out geogrids equipped with anchor system in a large device where the displacements of geogrid ribs were measured using linear variable differential transformers (LVDTs). Pinho-Lopes et al. (2016) performed pullout tests on exhumed geotextiles and geogrids using linear potentiometers to assess measurements of internal displacements. These commonly used instruments have various limitations, however. In the first place, when an extensometer, a traditional instrument for deformation measurements, is applied to the measurement of geosynthetics in soil, interactions can be easily affected by dimension and the installation of the extensometer. Strain gauges typically should not be loaded beyond their design limits, and engineering practice suggests that this is 3000 με, inadequate to cover the large deformation of geosynthetics. In many cases there is also a mismatch between the stiffness of a strain gauge and reinforcement such that these introduce a significant observer-effect. LVDTs can only operate with a power supply, something which might not be convenient for field life cycle monitoring. An FBG is a high precision instrument with excellent reliability and communication. As an optical fiber is the core component of FBG, the FBG is fragile and usually requires extra protection in engineering practice. In recent years, due to improvements in computer technology, various types of digital image analysis systems have been employed (Zhou et al., 2012; Bathurst and Ezzein, 2016, 2017). Similar analysis systems are expensive and their installation is quite complicated and requires sufficient space, which means that these systems are inconvenient for in-situ tests. A novel concept of sensor-enabled geosynthetics (SEGs) based on the piezoresistivity of electrically filled polymers was developed by Hatami et al. (2009), while Cui et al. (2018) improved the manufacturing process and successfully produced commercial sensor-enabled geobelts (SEGBs). The tensoresistivity performance of SEGBs means that it is easy to utilize these to analyze the deformations of geosynthetics in soil.

As the reinforcing effect of geosynthetics in soil structures is a result of interactions between these compounds and the surrounding soil, pullout tests are often considered as one of the most effective methods for studying the deformation behaviour of geosynthetics in soil structures. The scheme in Fig. 1 shows a reinforced retaining wall; in this example, failure may occur along the potential plane inside the retaining wall. Thus, once a potential failure plane begins to develop, the interaction between soil and

geosynthetics near to this line can be regarded as a pullout test for geosynthetic reinforcement. A failure mode for geosynthetic reinforcement might be regarded as an equivalent pullout test, and thus the potential for geobelt tensile failure or pullout, as force is developing to resist the otherwise significant potential movement along the potential failure plane, is significantly related to stability of the geosynthetic reinforced soil structure.

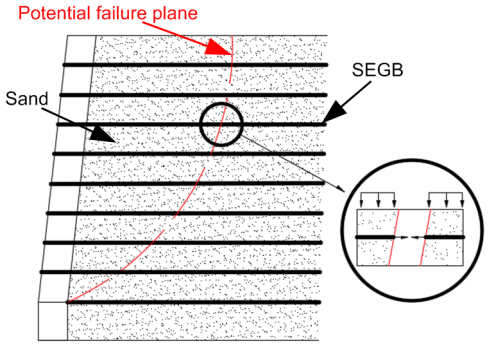

Fig. 1 A potential failure plane in a reinforced retaining wall

Numerous researchers have reported pullout tests on different geosynthetics or analyzed the results of these approaches. Rousé et al. (2014) reported pullout tests on geomembranes and calculated resistance using a back-analysis method, while Benessalah et al. (2016) conducted compressive triaxial tests and studied the reinforcement of geotextiles on shear strength responses in sand. In another study, Cardile et al. (2017) analyzed the interaction between soil and the transverse ribs of geogrids, considering soil dilatancy and interference phenomena for closely spaced bearing members. The majority of analyses to address pullout tests have focused on the deformation behaviour of geosynthetics under different conditions, such as confining pressure, specimen length and width, and soil type.

Despite a large body of research that has been published dealing with reinforced soil, there is a paucity of information addressing the deformation characteristics of geosynthetics considering failure modes (i.e. geobelt tensile failure or pullout) from the perspective of long-term monitoring of performance intended to allow assessment of how a structure behaves over time. The objective of this paper was therefore to firstly report a series of pullout tests on SEGB with various lengths in sand under different normal pressures and to discuss these in the context of long-term monitoring of reinforced soil structures. Secondly, this paper aims to proposing a method for preliminary prediction of failure mode (i.e. geobelt tensile failure and pullout) based on observed pre-failure behaviour.

2 SEGB

2.1 Basic concepts

The geobelt used in this study is an SEGB, a polymer composite made from high-density polyethylene (HDPE). Thus, by mixing a masterbatch of carbon black with HDPE, an SEGB exhibits conductivity and piezoresistivity. The concept of this composite material was developed by Hatami et al. (2009) who also demonstrated basic features (e.g. piezoresistivity) at the laboratory scale. Building on this, Cui et al. (2018) developed this concept and preliminary product to improve the manufacturing process for an SEGB. This paper reported pilot plant tests on mechanical and electrical properties. Thus, to enhance the friction between SEGB and soil, the texture of a specific belt tested was designed as a series of rhombuses with long and short diagonals of 4.0 mm and 1.5 mm, respectively (Fig. 2).

2.2 SEGB tensoresistivity

As a result of conductive carbon black dispersed in HDPE, SEGB exhibits tensoresistivity, which allows the evaluation of strains by measuring changes of electrical resistance. Tensoresistivity performance was investigated in slow tensile tests. Results show that normalized electrical resistance monotonically increased with strain. Cui et al. (2018) therefore suggested fitting normalized electrical resistance–strain curves with the following quadratic polynomial equation:

$$\frac{R_s}{R_0} = \alpha\varepsilon^2 + \beta\varepsilon + 1, \tag{1}$$

where ε is the strain in the SEGB (%), R_0 is the initial value of the electrical resistance (Ω), R_s is the measured value of electrical resistance after deformation

(Ω), and coefficients α and β are constants related to materials. In this case, α=0.01599 and β=0.1853.

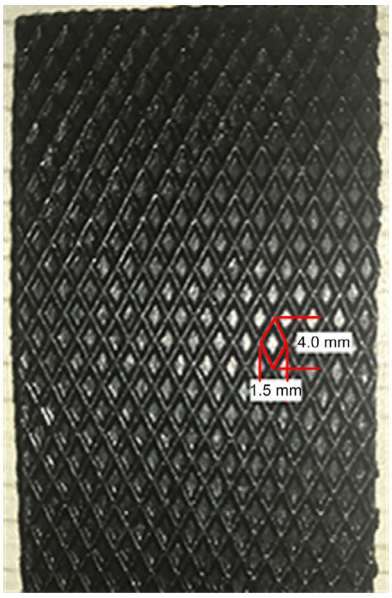

Fig. 2 Rhombus-shaped texture of the SEGB surface examined in this study

2.3 SEGB tensile properties

A series of uniaxial tensile tests were conducted as per ASTM D6637/D6637M (ASTM, 2015) to study the tensile properties of a 100 mm×25 mm×1.8 mm SEGB (at 1 mm/min). HDPE is a viscous material which exhibits predominantly visco-elasticity in the early stages of loading and predominantly visco-plasticity in later stages. Thus, when tensile strain was less than 4%, the specimen exhibited quasi-elasticity (visco-elasticity) and tensile stress increased almost linearly with strain with a scant stiffness (Fig. 3). However, when strain exceeded 4%, visco-plasticity began to dominate until stress reached a maximum value of 15 MPa at a strain of 15%. The specimen eventually underwent geobelt tensile failure at a strain of 27.6% and a tensile stress of 13 MPa. Geometrical and mechanical properties are tabulated in Table 1.

3 Preparation and pullout tests

3.1 Backfill soil

The dry sand used here was SP-SM (as per Unified Soil Classification System, ASTM D422-63) (ASTM, 2007) with d_{10}=0.23 mm, d_{30}=0.53 mm, d_{50}=0.95 mm, d_{60}=1.27 mm, curvature coefficient C_c=0.96, and uniformity coefficient C_u=5.52. d_{10}, d_{30}, d_{50}, and d_{60} refer to the diameters for which 10%, 30%, 50%, and 60% of the soil sample by weight pass the sieve mesh, respectively. The maximum and minimum dry densities of this material are 1920 kg/m^3 and 1395 kg/m^3, respectively.

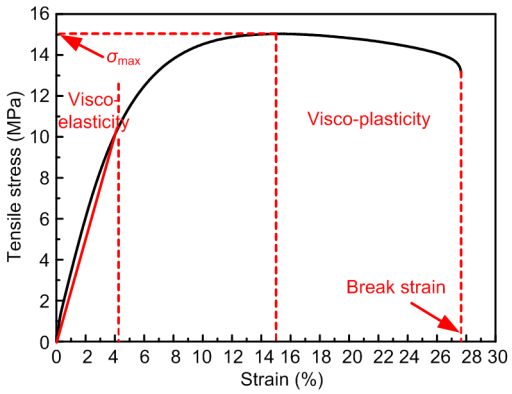

Fig. 3 Stress–strain curve of tensile tests at 1 mm/min of examined SEGB (σ_{max} is the peak tensile stress)

Table 1 Geometrical and mechanical properties of SEGB

Property	Value
Mass per unit area (kg/m^2)	1.48
Tensile strength (MPa)	15.0
Thickness (mm)	1.8
Tensile stress (2% strain) (MPa)	6.1
Breaking elongation (%)	27.6

3.2 Test specimen preparation

The SEGB specimens used here were 40-mm wide and 1.8-mm thick (Fig. 4). The lengths of specimens examined were 20 cm, 30 cm, 40 cm, 50 cm, and 60 cm, respectively. By attaching wires, electrical resistance between two adjacent attached nodes was measured. The distance between two adjacent nodes was then selected considering the length of each specimen and the number of attached nodes but usually ranged from 4 cm to 6 cm. Attached nodes were then encircled with conductive adhesive tapes, and electrical resistance values were measured between adjacent measurement points once every 2 min.

3.3 Pullout test device

A pullout device (Fig. 5) has four components, a test box, a horizontal pulling system, a vertical

loading system, and a force sensor system. An SEGB specimen was embedded in compacted sand in an 800 mm (long)×400 mm (wide)×550 mm (high) test box. The front end of the SEGB specimen extended through an aperture in the front wall of the test box (Fig. 6) and was fixed on a clamp. In order to prevent soil particles running through the aperture, a restraint was placed on the inner side of the front wall. The inner sides of the sidewalls were then greased and covered with plastic film to reduce friction due to soil particles.

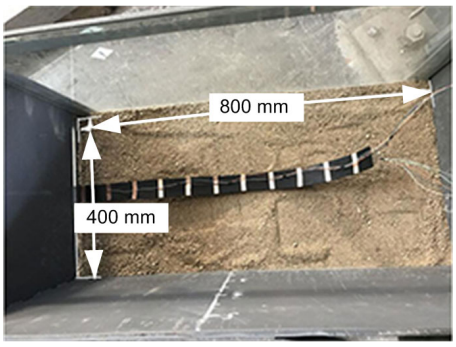

Fig. 6 A test specimen for a pullout test in place

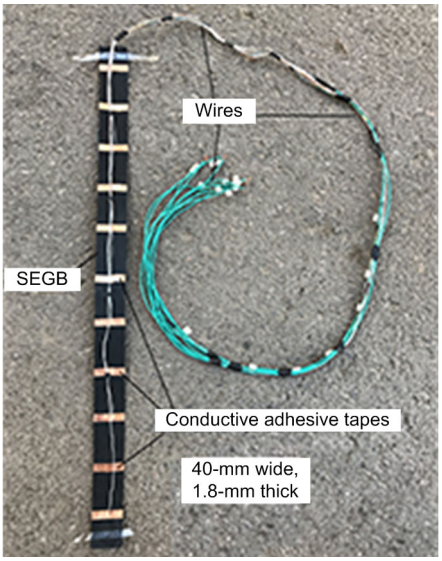

Fig. 4 An SEGB specimen with wires and conductive adhesive tapes attached. Modified from (Cui et al., 2019), Copyright 2019, with permission from Elsevier

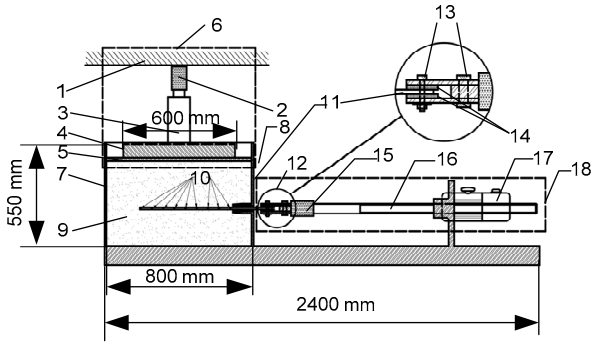

Fig. 5 Schematic of pullout test apparatus

1: reaction frame; 2: pressure sensor; 3: hydraulic jack; 4: I-beam; 5: bearing plate; 6: vertical loading system; 7: test box; 8: restraint; 9: soil; 10: conductive adhesive tapes; 11: SEGB; 12: clamp; 13: high-strength bolts; 14: rubber sheet; 15: tensor sensor; 16: screw; 17: electric servomotor; 18: horizontal pulling system. Modified from (Cui et al., 2019), Copyright 2019, with permission from Elsevier

The system used for applying pulling load to the SEGB involved a screw powered by an electric servomotor. A servomotor ensured that the clamp moved at a constant displacement rate set at 1.0 mm/min as per ASTM D6706-01 (ASTM, 2013). The SEGB was then clamped between two rubber sheets which were held between two steel plates by five high-strength bolts. No SEGB specimens broke inside the clamps suggesting that this system does not influence the validity of results.

The vertical loading system used here comprised a hydraulic jack attached to the reaction frame at one end and two I-beams at the other. Two I-beams with a length of 60 cm were then deployed abreast of one another on a bearing plate to apply a normal pressure as uniformly as possible. The bearing plate is a 10-mm thick steel plate that covers the test box.

The force sensor system used here comprised two components. One monitored the tension induced by the screw in the horizontal pulling system while the other was attached to a vertical loading system to monitor the pressure from hydraulic jacks.

3.4 Procedures and pullout test cases

Pullout test procedures strictly followed ASTM D6706-01. The sand was compacted to a desired relative density of 90% by layers with thickness of 50 mm. Sand layers were then compacted with a handheld hammer and the surface was leveled with a spatula. Layers were compacted in the lower half of the pullout box until the surface was slightly above the bottom edge of the aperture on the box. An SEGB specimen was then placed on the leveled sand surface. The pullout end of the specimen stretched through the aperture and was connected to the clamp and wires on

the SEGB specimen led out of pullout box. The specimen and the clamp system were connected to one another firmly without damaging the specimen, and a set position of the latter was used to guarantee the length of the specimen inside the box reached the desired effective length. The top half of the sand was then compacted in the same way to the desired relative density of the bottom half. Normal pressure was then applied before the test was initiated. Pullout tests were terminated once either tensile failure or pullout has occurred.

In terms of the effective length of specimens, sufficiently high normal pressure was applied to ensure that geobelt tensile failure occurred near to the box aperture. This was then decreased in subsequent tests until the specimen reached pullout. These cases were carried out twice with the same normal pressure and effective specimen length to eliminate the influence of material variability on test results. Test results of these pullout cases were average values of two iterations.

Test cases were named using the format 'LxxPxx', where 'Lxx' represent the length of SEGB in cm and 'Pxx' the normal pressure in kPa. Thus, for example, L60P05 denotes a test on a 60-cm long SEGB specimen at a normal pressure of 5 kPa.

4 Analysis of pullout test results

4.1 Front pullout tensile stress–front displacement curves under two failure modes

A series of pullout SEGB tests were conducted (Table 2) and failure modes were noted for each specimen length and applied normal pressure (i.e. geobelt tensile failure or pullout) (Table 3).

Table 2 Cases examined in this study

Effective length, l (cm)	Normal pressure, σ_v (kPa)
20	50, 45, 40, 35, 30
30	30, 25, 20
40	20, 15, 10
50	10, 5
60	10, 5

In cases where geobelt tensile failure was the primary mode, pullout tensile stresses increased to a peak of approximately 15 MPa as indicated by the straight line (Fig. 7a). The higher the normal pressure, the faster the front pullout tensile stress reached this peak value. Results show that front displacement at geobelt tensile failure generally increased with specimen length while it decreased with increasing normal pressure given the same dimension.

Table 3 Failure modes observed in tests

Effective length, l (cm)	Normal pressure, σ_v (kPa)	Failure mode	Peak tensile stress (MPa)
20	45	Tensile failure	15.3
20	35	Tensile failure	15.4
20	30	Pullout	9.8
30	30	Tensile failure	15.4
30	25	Tensile failure	15.1
30	20	Pullout	13.0
40	20	Tensile failure	15.6
40	15	Tensile failure	15.2
40	10	Pullout	14.3
50	10	Tensile failure	14.9
50	5	Pullout	14.6
60	10	Tensile failure	15.2
60	5	Pullout	14.7

Pullout tensile stress–displacement curves were obtained easily from tests and reflect interactions between geobelts and confining sand. The geobelt–sand interaction was closely related to failure mode. Pullout tensile stress–displacement curves of SEGB differed substantially depending on whether the failure mode was in geobelt tensile failure (Fig. 7a) or pullout (Fig. 7b). Indeed, in cases where failure was due to geobelt tensile failure, pullout tensile stress increased monotonically with front displacements until tensile strength (about 15 MPa) was reached and remained relatively constant thereafter until tensile break occurred or the test was terminated. In most cases, the ultimate constant value was close to 15 MPa and indicates that full tensile capacity could be mobilized although it is also the case that the lower the normal stress the more the displacement required to mobilize the full load. At the same time, the longer the reinforcement the lower the normal stress needed to mobilize full tensile capacity. In cases L20P30, L30P20, L40P10, L50P5, and L60P5, full mobilization was not possible (Fig. 7b) although pullout tensile stresses in the latter two were close to tensile

capacity. Comparing geobelt tensile failure case L20P35 in Fig. 7a, it is possible to infer that the minimal normal pressure inducing the failure mode of geobelt tensile failure is close to 35 kPa.

Front pullout tensile stress–displacement curves under both failure modes are shown in Fig. 7c. In these examples, front displacements are normalized by length of specimens to make cases comparable. Peak values for all tensile failure mode cases (lines with solid symbols in Fig. 7c) occurred at around 5% of normalized front displacement. Thus, at a given normal pressure for the geobelt and sand tested, specimens reached material tensile strength when front displacement reached about 5% of the specimen length. Geobelt failure mode in specific pullout cases can therefore be predicted on the basis of pullout tensile stress when the front displacement reached 5% of specimen length. Thus, if pullout tensile stress reached that of the specimen (15 MPa in these cases), the failure mode is prone to be tensile failure.

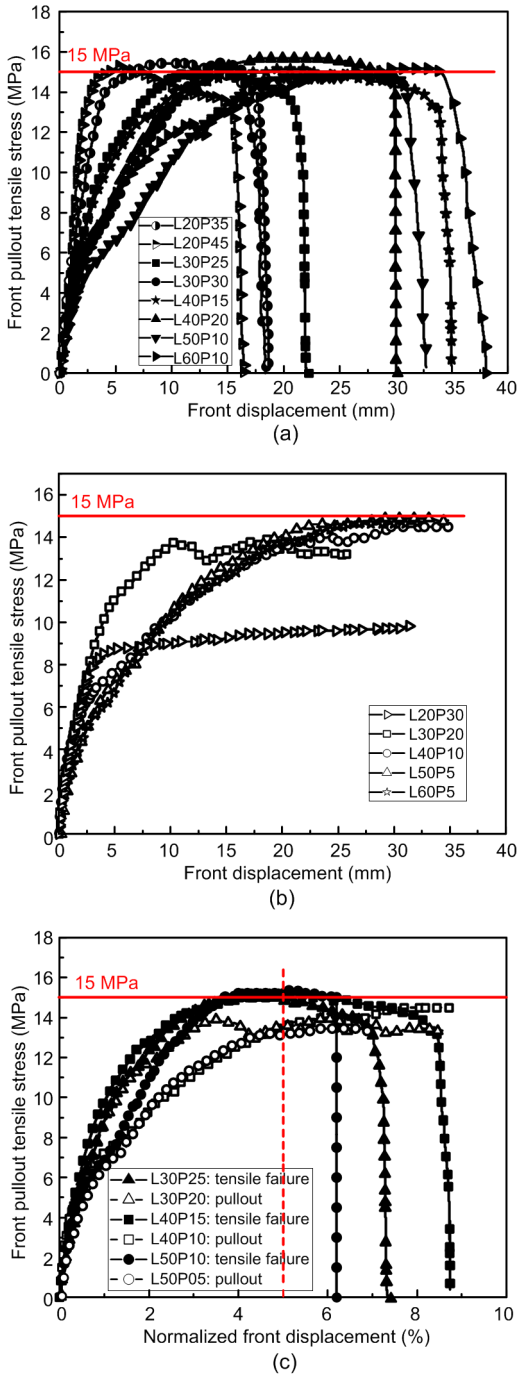

Fig 7 Pullout test results: (a) tensile failure; (b) pullout; (c) normalized results for two failure modes

4.2 A critical line between two failure modes

The critical normal pressure (i.e. the normal pressure at which there is a transition between geobelt tensile failure and pullout) for a geosynthetic specimen of a given length is indicated in Fig. 8. The critical line can be described for this case as follows:

$$\sigma_v = a + b\mathrm{e}^{-cl}, \tag{2}$$

where a, b, and c are related parameters with a=2.0 kPa, b=83.83 kPa, and c=0.05 m^{-1}.

The area above this critical line corresponds to the geobelt tensile failure zone while the area below corresponds to that for pullout. This critical line can be used as a map or index for preliminary judgement about failure mode as it simply depends on length and confining pressure. Although derived from pullout tests, the critical line was applicable for geosynthetics-reinforced structures (Fig. 1). It should be noted that the parameters in Eq. (2) are only effective for specific geobelt, sand, and compaction degree, however.

The critical line in Fig. 8 obviously indicates that critical normal pressure decreases as specimen length increases. Critical normal pressure corresponds to a normal pressure under which failure mode is a transition between tensile failure and pullout. No matter which failure mode is developed then, geobelt failure in a pullout test is actually a state of limit equilibrium between the fracture energy of a specimen and the work of pullout force. The fracture energy of specimen, denoted by V_s, is a constant in these tests when loading rate and specimen dimensions remain unchanged. The work of pullout force, W_f, is very

significantly related to the interfacial shear response, described as

$$W_{\mathrm{f}}=\int_0^{u_{\mathrm{m}}}F_{\mathrm{f}}\mathrm{d}u=A_{\mathrm{s}}\int_0^{u_{\mathrm{m}}}\tau\left(\sigma_{\mathrm{v}},c_{\mathrm{sg}},\varphi_{\mathrm{sg}}\right)\mathrm{d}u$$
$$=2Bl\int_0^{u_{\mathrm{m}}}\tau\left(\sigma_{\mathrm{v}},c_{\mathrm{sg}},\varphi_{\mathrm{sg}}\right)\mathrm{d}u, \quad (3)$$

where F_{f} is the front pullout force (N), u is the front displacement (m), u_{m} is the maximum front displacement corresponding to failure (m), A_{s} is the interfacial shear area (m^2), and τ is the interfacial shear stress (Pa), a function of multiple variables such as normal pressure σ_{v} (Pa), interfacial cohesion c_{sg} (Pa), and interfacial friction angle φ_{sg} (°). B is the specimen width (m).

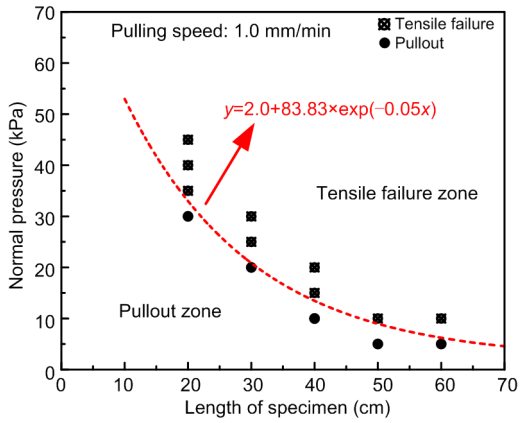

Fig. 8 Critical line between two failure modes in pullout tests

It is the case that if $W_{\mathrm{f}}<V_{\mathrm{s}}$, pullout force is unable to mobilize the full tensile capacity of a specimen then this will result in pullout mode. Similarly, when $W_{\mathrm{f}}>V_{\mathrm{s}}$, the failure mode is tensile failure, but when $W_{\mathrm{f}}=V_{\mathrm{s}}$, the failure mode is in transition corresponding to the critical line. Thus, on the basis of Eq. (3), if the effective length of specimen l increases, the constant V_{s} requires decreasing interfacial shear stress τ, and normal pressure σ_{v} consequently decreases.

5 Analysis of SEGB self-measurement results

The following sections of this paper are focused on the analysis of pullout tests in terms of strain, stress, and displacement distribution in cases L40P10 and L40P15 where failure modes are pullout and tensile failure, respectively. Thus, in the case of L40P10 (Fig. 9), front pullout tensile stress monotonically increased with front displacement and then remained constant at the maximum value until the specimen was pulled out. In comparison, front pullout tensile stress for L40P15 reached a peak value earlier than that for L40P10 as the geobelt experienced tensile failure as seen in L40P15 (Fig. 9).

Three representative points in load–displacement history (denoted by moments A, B, and C in Fig. 9) were selected for time at which the strain distribution along the geobelt could be compared. Moment A denotes the point at which the load–displacement curve at the front departs from quasi-linearity, while moment B corresponds to when the geobelt reaches its tensile capacity (i.e. front pullout tensile stress approaches the maximum value). Finally, moment C denotes the point at which front displacement is 2 mm before geobelt tensile failure.

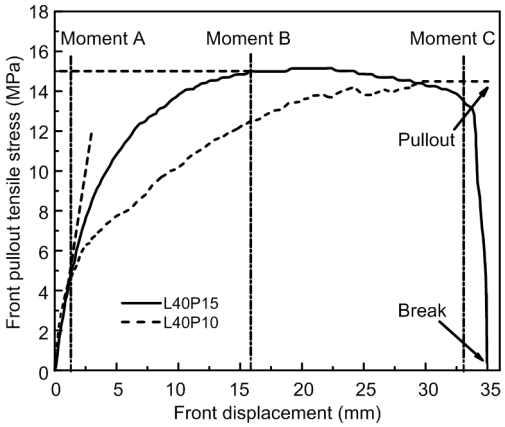

Fig. 9 Front pullout tensile stress–front displacement relations for SEGB under two failure modes

5.1 Strain distribution in pullout process

Real-time self-measurements obtained from SEGB provided strain distribution along the geobelt inside soil during the entire pullout test. Thus, each strain was shown as a midpoint of each measure zone at 5 cm to indicate that strain was essentially an average value as calculated using Eq. (1). Fig. 10 shows the strain distribution for the two cases at three moments. The positions at which self-measurement strains were recorded were normalized by the specimen's length, 40 cm. Data show that during the

pullout test for L40P15 (the case with geobelt tensile failure in Fig. 10), calculated strain at 5% corresponds to moment A, the onset of non-linearity at the front end. Secondly, a calculated strain of 15.9% corresponds to the peak value of pullout force at moment B, while a calculated strain of 27.6% corresponds to the geobelt tensile break at moment C. This break occurred on SEGB at the aperture of test box, consistent with findings from tensile properties observed from a uniaxial tensile test (Fig. 3).

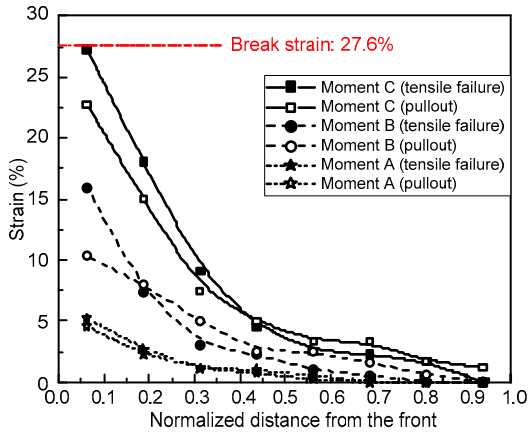

Fig. 10 Strain distributions along the specimen in cases L40P10 and L40P15 at three moments in load–displacement history

Although the magnitudes of strains at three moments are different in the test, the strain distributions follow a similar trend (Fig. 10). Mobilization of strain was transferred from the front end of the specimen to the tail end. Strain magnitudes decreased rapidly within the range (0–30%) close to the front end, and declined slowly afterwards.

On the basis of the tensile properties of SEGB in Fig. 3, the strain at geobelt tensile break is 27.6%. Indeed, when strain at the front end reaches the geobelt tensile break level, a specimen will break at the front. A similar observation can be seen for all other cases where failure was due to a break in the geobelt.

Strain at the very end of the geobelt must be zero in all cases. This stain is averaged over a distance of 5 cm. Thus, in all cases, the last reported strain for cases where failure mode was geobelt tensile failure was negligible, while in cases with the failure mode of pullout, zero strain was partly observed at the tail end in some cases. Zero strain in the tail zone means that this region of the specimen has not yet been mobilized by soil interaction, and there is still potential of mobilization under larger pullout force as long as tensile limit of material is not reached.

5.2 Stress distribution in pullout process

Utilizing the full stress–strain curve in Fig. 3 as an index, stresses along the specimen at all three moments (Fig. 11) were calculated according to measured strains (Fig. 10). Similar to the strain distribution, mobilization of stress was generally transferred from the front end of the specimen to the tail end except for the fact that stress slightly increased between the two measurement points close to the front zone at moment C. This exception is because plastic strains were developed in the specimen as the tensile strength was reached and the geobelt experienced some apparent strain softening before its tensile break occurred (Fig. 3).

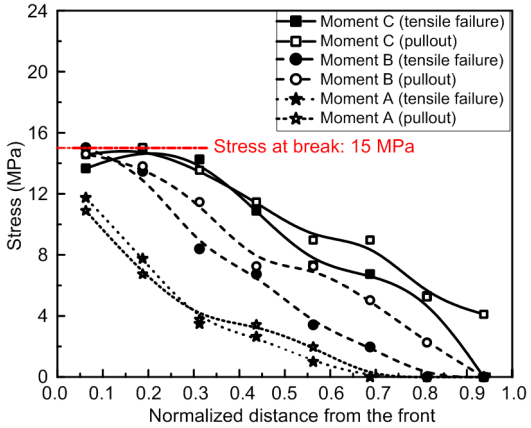

Fig. 11 Stress distributions along the specimen in cases L40P10 and L40P15 at three moments in load–displacement history

5.3 Displacement distribution in pullout process

Wall monitoring mostly includes the displacement of wall facing (or lateral displacement) as well as soil settlement. Failure usually derives from internal damage; as this accumulates and links through, a failure plane gradually develops and external damage can be observed. It is therefore inadequate to prejudge failure plane simply by monitoring external displacements such as lateral ones and settlements. Fig. 1 illustrates the connections between the pullout behavior of geobelts and the failure plane. The displacement of geobelts in the pullout process therefore needs to be discussed.

Displacement distribution along the specimen can be acquired via simple calculation based on strain distribution (Fig. 12). The average strain of the ith measure zone (ε_i) can be defined as

$$\varepsilon_i = \frac{u_{i-1} - u_i}{\Delta l}, \tag{4}$$

where u_{i-1} and u_i denote the displacements of the two ends of the ith measure zone, and Δl is the distance between the two ends (the length of the ith measure zone).

Front displacement u_0 was given on the basis of pullout test results, while the displacements u_i of other measurement points can be calculated progressively according to strain distribution.

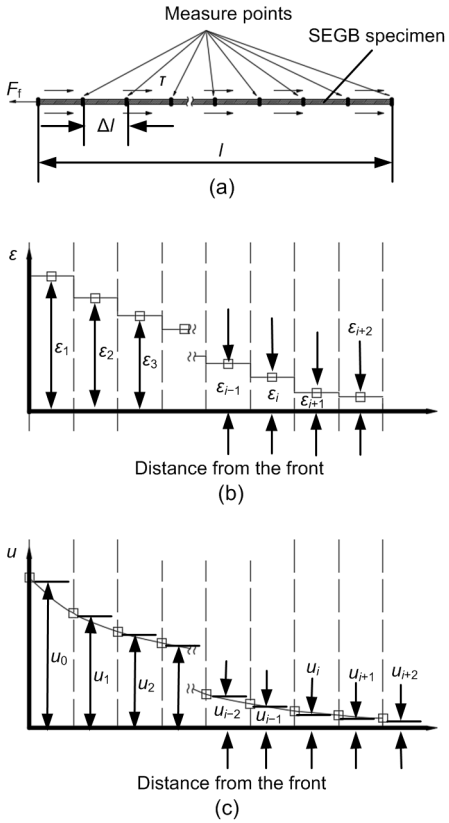

Fig. 12 Relationship between the distribution of average strain and displacement: (a) SEGB specimen with measure points in pullout tests; (b) average strain distribution along the SEGB specimen; (c) displacement distribution along the SEGB specimen

The displacement distribution (Fig. 13) along the specimen is similar to that of strain. This means that the mobilization of displacement was transferred from the front end to the tail end along the specimen. Indeed, displacement decreased rapidly within the range close to the front end and then decreased slowly and steadily. Compared with cases in the failure mode of geobelt tensile failure, displacements for cases in the failure mode of pullout were generally larger. In the early period of pullout process (moment A), few differences between displacements were seen in the two cases. As front displacements increased, the displacements in the pullout case increased faster than those in the tensile failure case. The displacement in the tensile failure case at moment C remained small at the tail end while the displacement in the pullout case was obviously larger (Fig. 13).

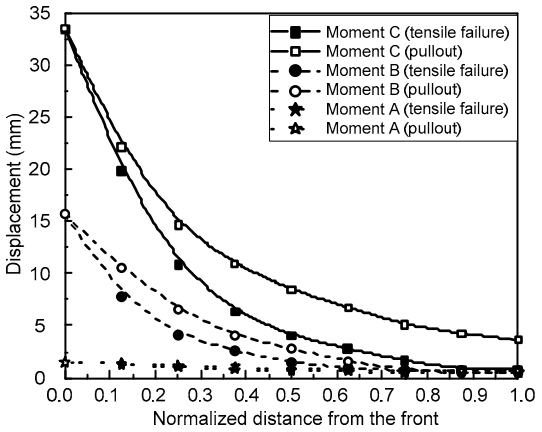

Fig. 13 Displacement distributions along the specimen in cases L40P10 and L40P15 at three moments in load–displacement history

The specimen displacement distribution in the pullout process clearly shows that this variable decreased rapidly from the failure plane (front displacement in pullout process) towards the facing wall (tail displacement in pullout process). As external wall deformations were observed, geobelts might exhibit large displacements near the failure plane. It is too late to prejudge the failure plane simply by monitoring external deformations.

6 SEGB failure mode criteria

As failure plane develops in a reinforced wall, the interaction between soil and geosynthetics near to the failure plane can be regarded as pullout tests on

geosynthetics. The largest strain usually occurred in the geosynthetics near the failure plane, resembling two pullout tests linking up. Benefitting from the self-measurement of SEGB, the strain distribution along the geobelts inside soil could be obtained as shown in Fig. 14. Based on the aforementioned analyses on pullout tests, a method for predicting failure plane and proposing warning criteria for SEGB failure modes could be provided.

Once the strain distribution along the geobelt reached a peak value, the potential failure plane could be prejudged. A geobelt can be divided by the potential failure plane into two parts with lengths l_1 and l_2, respectively, as shown in Fig. 14. Combining the geobelt length and the corresponding confining pressure, the failure mode of the geobelt could be preliminarily predicted according to Eq. (2) or Fig. 8.

As the failure plane was developing, the peak value of strain distribution increased and the mobilization of the strain was transferred from the failure plane to either side along the geobelt. The strain and displacement at tail zones of geobelts must be closely concerned. At the beginning, the strains at tail zones should be zero. Once the strains at tail zones were no longer zero, the geobelts were prone to be pulled out. If the strains at tail zones remained to be zero but the peak strain at failure plane reached the level of tensile strength of specimens, the geobelts were prone to be tensile failure eventually.

The proposed warning criteria for failure modes of SEGB may still have some limitations considering that SEGB is a polymer composite made from HDPE, which is a viscoelastic material and the stress and stain will change with time (relaxation and creep, for example). Therefore, the pullout behaviour of SEGB considering several different rates and aging should be investigated in the follow-up research.

7 Discussion

It should be noted that pullout test results could be influenced by the boundary conditions of test device, especially the clamping system and specimen width.

ASTM D6706-01 (ASTM, 2013) suggests a clamping device as Fig. 15 shows, including metal sleeves and clamps stretching into test box. The metal sleeves at the entrance to the test box function to transfer force into the soil to a sufficient horizontal distance so as to significantly reduce the stress on the front door of the box. The absence of metal sleeves in this study would result in higher test results in two aspects. One is the exposure of front part of specimens to the air when specimens were pulled out from test box. The unconfined surroundings obviously could cause larger deformation of specimen's front end. The other aspect is the stress concentration on front door of test box during the pullout process. Soil particles near the geobelt–soil interfaces move in pullout direction under interfacial shear stress, resulting in stress concentration on front door of box and redistribution of normal pressure along the interfaces. Without metal sleeves in test box, the stress concentration would lead to the increment of normal pressure on the geobelt specimens near the entrance, which would result in higher pullout force.

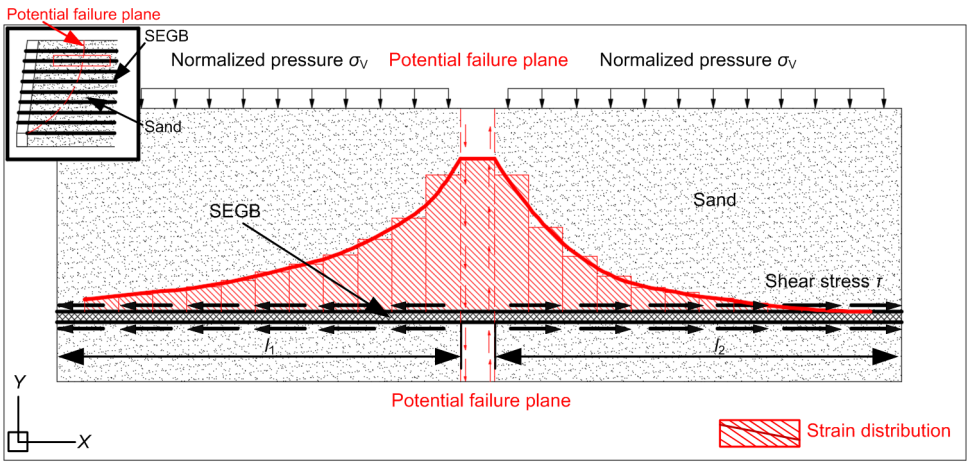

Fig. 14 Data viewed from perspective of a point near the failure plane in Fig. 1

The width of specimens also has influence on test results. Theoretical and experimental studies (Hayashi et al., 1996; Ghionna et al., 2001; Moraci and Recalcati, 2006) have reported that when the width of reinforcement specimens is smaller than the width of the box, soil dilatancy increases in the upper and lower areas of the reinforcement specimen as Fig. 16a shows. Non-dilating zones in the soil surroundings restrain soil dilatancy in dilating zones.

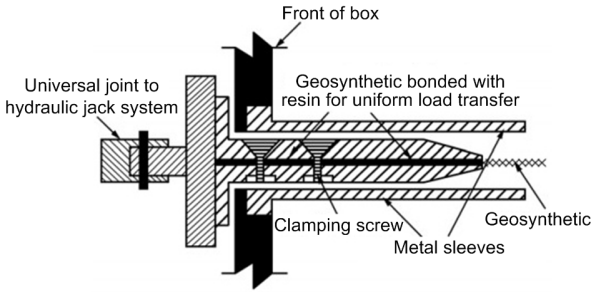

Fig. 15 A suggested clamping device (ASTM D6706-01)
Reprinted from (ASTM, 2013), Copyright 2013, with permission from ASTM

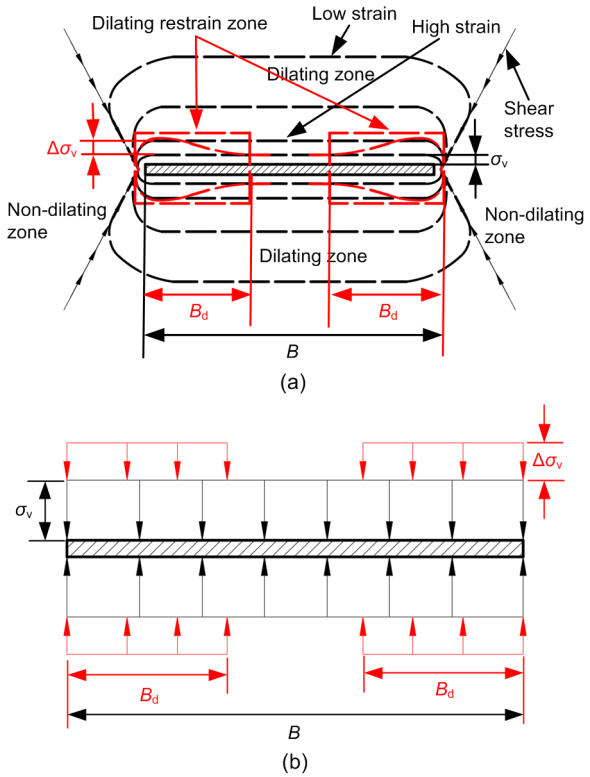

Fig. 16 Boundary effects of specimen width on pullout resistance: (a) dilating and non-dilating zones on width; (b) redistribution of normal pressure induced by soil dilatancy (*B* is the specimen width; B_d is the restrained dilatancy width developed at both edges of the specimen)

The restraint generates shear stresses at the border between the dilating and non-dilating zones, and produces an increment of the normal pressure $\Delta\sigma_v$ on geobelt–soil interfaces (as illustrated in Fig. 16b). For the specimens having a width smaller than test box, the dilating restrained zones will influence the redistribution of normal pressure on specimen width. Although ASTM D6706-01 recommends the minimum distance between the specimen and the side wall to be 150 mm to eliminate sidewall friction effect, the smaller specimen width would result in higher increment of the normal pressure $\Delta\sigma_v$ induced by soil dilatancy, and consequently higher pullout resistance.

The boundary conditions of the pullout test device would overestimate pullout test results, which has been proved by the comparison of numerical and test results (Cui et al., 2019, 2020). Such overestimation would result in higher pullout forces for the pullout cases, and smaller pullout displacements for the tensile failure cases. Further studies on the boundary conditions of pullout test device are worthwhile.

8 Conclusions

A series of pullout tests on SEGB were reported. SEGBs with various lengths were pulled out from sand under different normal pressures to study the two failure modes: geobelt tensile failure and pullout. The deformation characteristics in these two failure modes were discussed in terms of strain, stress, and displacement distributions along the SEGB. For the conditions examined, it can be concluded that:

1. A critical line considering the length of SEGB and confining pressure was proposed to describe the transition between two failure modes: geobelt tensile failure and pullout. The critical line could be utilized for preliminary prediction of failure mode of SEGB.

2. On the basis of strain distribution from the self-measurement of SEGB, warning criteria for the failure modes of SEGB were established. The strain distribution along the geobelt showed a peak value where the potential failure plane occurred, and the mobilization of the strain was transferred from the failure plane to either side. Once the strains at tail zones were no longer zero, the geobelts were prone to be pulled out. If the strains at tail zones remained to

be zero but the peak strain at failure plane reached the level of tensile strength of specimens, the geobelts were prone to be tensile failure eventually. The warning criteria could be utilized for preliminary recognition and judgment of the potential failure modes during service life.

Acknowledgements

The authors appreciate the constructive comments and suggestions made by Prof. Ronald Kerry ROWE (Queen's University, Canada) which improved the draft of this paper.

Contributors

Xin-zhuang CUI designed the research. Yi-lin WANG carried out the tests, processed the corresponding data, and finished the first draft of the manuscript. Kai-wen LIU helped to organize the manuscript. Yi-lin WANG and Kai-wen LIU revised and edited the final version.

Conflict of interest

Yi-lin WANG, Xin-zhuang CUI, and Kai-wen LIU declare that they have no conflict of interest.

References

Allen TM, Bathurst RJ, 2014. Performance of an 11 m high block-faced geogrid wall designed using the K-stiffness method. *Canadian Geotechnical Journal*, 51(1):16-29. https://doi.org/10.1139/cgj-2013-0261

ASTM (American Society for Testing and Materials), 2007. Standard Test Method for Particle-size Analysis of Soils, ASTM D422-63(2007)e2. ASTM International, West Conshohocken, USA.

ASTM (American Society for Testing and Materials), 2013. Standard Test Method for Measuring Geosynthetic Pullout Resistance in Soil, ASTM D6706-01(2013). ASTM International, West Conshohocken, USA.

ASTM (American Society for Testing and Materials), 2015. Standard Test Method for Determining Tensile Properties of Geogrids by the Single or Multi-rib Tensile Method, ASTM D6637/D6637M-15. ASTM International, West Conshohocken, USA.

Bathurst RJ, Ezzein FM, 2016. Geogrid pullout load-strain behaviour and modelling using a transparent granular soil. *Geosynthetics International*, 23(4):271-286. https://doi.org/10.1680/jgein.15.00051

Bathurst RJ, Ezzein FM, 2017. Insights into geogrid-soil interaction using a transparent granular soil. *Géotechnique Letters*, 7(2):179-183. https://doi.org/10.1680/jgele.16.00191

Benessalah I, Arab A, Villard P, et al., 2016. Shear strength response of a geotextile-reinforced Chlef sand: a laboratory study. *Geotechnical and Geological Engineering*, 34(6):1775-1790. https://doi.org/10.1007/s10706-016-9988-7

Cardile G, Gioffrè D, Moraci N, et al., 2017. Modelling interference between the geogrid bearing members under pullout loading conditions. *Geotextiles and Geomembranes*, 45(3):169-177. https://doi.org/10.1016/j.geotexmem.2017.01.008

Chaiyaput S, Bergado DT, Artidteang S, 2014. Measured and simulated results of a Kenaf limited life geosynthetics (LLGs) reinforced test embankment on soft clay. *Geotextiles and Geomembranes*, 42(1):39-47. https://doi.org/10.1016/j.geotexmem.2013.12.006

Chen RP, Wang YW, Ye XW, et al., 2016. Tensile force of geogrids embedded in pile-supported reinforced embankment: a full-scale experimental study. *Geotextiles and Geomembranes*, 44(2):157-169. https://doi.org/10.1016/j.geotexmem.2015.08.001

Cui XZ, Cui SQ, Jin Q, et al., 2018. Laboratory tests on the engineering properties of sensor-enabled geobelts (SEGB). *Geotextiles and Geomembranes*, 46(1):66-76. https://doi.org/10.1016/j.geotexmem.2017.10.004

Cui XZ, Wang YL, Liu KW, et al., 2019. A simplified model for evaluating the hardening behaviour of sensor-enabled geobelts during pullout tests. *Geotextiles and Geomembranes*, 47(3):377-388. https://doi.org/10.1016/j.geotexmem.2019.01.007

Cui XZ, Wang YL, Liu KW, et al., 2020. Strain-softening model evaluating geobelt–clay interaction validated by laboratory tests of sensor-enabled geobelts. *Canadian Geotechnical Journal*, 57(3):354-365. https://doi.org/10.1139/cgj-2018-0560

Ghionna VN, Moraci N, Rimoldi P, 2001. Experimental evaluation of the factors affecting pull-out test results on geogrids. Proceedings of the International Symposium on Earth Reinforcement.

Gurung N, 2001. 1-D analytical solution for extensible and inextensible soil/rock reinforcement in pull-out tests. *Geotextiles and Geomembranes*, 19(4):195-212. https://doi.org/10.1016/S0266-1144(01)00008-5

Hatami K, Grady BP, Ulmer MC, 2009. Sensor-enabled geosynthetics: use of conducting carbon networks as geosynthetic sensors. *Journal of Geotechnical and Geoenvironmental Engineering*, 135(7):863-874. https://doi.org/10.1061/(ASCE)GT.1943-5606.0000062

Hayashi S, Alfaro MC, Watanabe K, 1996. Dilatancy effects of granular soil on the pullout resistance of strip reinforcement. Proceedings of the International Symposium on Earth Reinforcement, p.39-44.

King DJ, Bouazza A, Gniel JR, et al., 2017a. Load-transfer platform behaviour in embankments supported on semi-rigid columns: implications of the ground reaction curve. *Canadian Geotechnical Journal*, 54(8):1158-1175. https://doi.org/10.1139/cgj-2016-0406

King DJ, Bouazza A, Gniel JR, et al., 2017b. Serviceability design for geosynthetic reinforced column supported embankments. *Geotextiles and Geomembranes*, 45(4):261-279. https://doi.org/10.1016/j.geotexmem.2017.02.006

King DJ, Bouazza A, Gniel JR, et al., 2018. Geosynthetic reinforced column supported embankments and the role of ground improvement installation effects. *Canadian Geotechnical Journal*, 55(6):792-809. https://doi.org/10.1139/cgj-2017-0036

Liu HB, 2016. Nonlinear elastic analysis of reinforcement loads for vertical reinforced soil composites without facing restriction. *Journal of Geotechnical and Geoenvironmental Engineering*, 142(6):04016013. https://doi.org/10.1061/(ASCE)GT.1943-5606.0001464

Liu HB, Yang GQ, Hung C, 2017. Analyzing reinforcement loads of vertical geosynthetic-reinforced soil walls considering toe restraint. *International Journal of Geomechanics*, 17(6):04016140. https://doi.org/10.1061/(ASCE)GM.1943-5622.0000840

Liu HB, Hung C, Cao JZ, 2018. Relationship between Arias intensity and the responses of reinforced soil retaining walls subjected to near-field ground motions. *Soil Dynamics and Earthquake Engineering*, 111:160-168. https://doi.org/10.1016/j.soildyn.2018.04.022

Luo N, Bathurst RJ, 2018. Deterministic and random FEM analysis of full-scale unreinforced and reinforced embankments. *Geosynthetics International*, 25(2):164-179. https://doi.org/10.1680/jgein.17.00040

Mehrjardi GT, Ghanbari A, Mehdizadeh H, 2016. Experimental study on the behaviour of geogrid-reinforced slopes with respect to aggregate size. *Geotextiles and Geomembranes*, 44(6):862-871. https://doi.org/10.1016/j.geotexmem.2016.06.006

Moraci N, Recalcati P, 2006. Factors affecting the pullout behaviour of extruded geogrids embedded in a compacted granular soil. *Geotextiles and Geomembranes*, 24(4):220-242. https://doi.org/10.1016/j.geotexmem.2006.03.001

Mosallanezhad M, Taghavi SHS, Hataf N, et al., 2016. Experimental and numerical studies of the performance of the new reinforcement system under pull-out conditions. *Geotextiles and Geomembranes*, 44(1):70-80. https://doi.org/10.1016/j.geotexmem.2015.07.006

Mousavi SH, Gabr MA, Borden RH, 2017. Optimum location of geogrid reinforcement in unpaved road. *Canadian Geotechnical Journal*, 54(7):1047-1054. https://doi.org/10.1139/cgj-2016-0562

Ni PP, Mei GX, Zhao YL, 2017. Displacement-dependent earth pressures on rigid retaining walls with compressible geofoam inclusions: physical modeling and analytical solutions. *International Journal of Geomechanics*, 17(6):04016132. https://doi.org/10.1061/(ASCE)GM.1943-5622.0000838

Pinho-Lopes M, Paula AM, Lopes ML, 2015. Pullout response of geogrids after installation. *Geosynthetics International*, 22(5):339-354. https://doi.org/10.1680/jgein.15.00016

Pinho-Lopes M, Paula AM, Lopes ML, 2016. Soil-geosynthetic interaction in pullout and inclined-plane shear for two geosynthetics exhumed after installation damage. *Geosynthetics International*, 23(5):331-347. https://doi.org/10.1680/jgein.16.00001

Rousé PC, Fannin RJ, Taiebat M, 2014. Sand strength for back-analysis of pull-out tests at large displacement. *Géotechnique*, 64(4):320-324. https://doi.org/10.1680/geot.13.T.021

Rowe RK, Liu KW, 2015. Three-dimensional finite element modelling of a full-scale geosynthetic-reinforced, pile-supported embankment. *Canadian Geotechnical Journal*, 52(12):2041-2054. https://doi.org/10.1139/cgj-2014-0506

Shi WZ, Peng FL, Kongkitkul W, 2016. FE simulation of rate-dependent behaviours of polymer geosynthetic reinforcements for an estimation of mobilized tensile force in a reinforced soil. *Computers and Geotechnics*, 80:49-58. https://doi.org/10.1016/j.compgeo.2016.06.005

Tran VDH, Meguid MA, Chouinard LE, 2013. A finite-discrete element framework for the 3D modeling of geogrid-soil interaction under pullout loading conditions. *Geotextiles and Geomembranes*, 37:1-9. https://doi.org/10.1016/j.geotexmem.2013.01.003

Wang ZJ, Jacobs F, Ziegler M, 2016. Experimental and DEM investigation of geogrid–soil interaction under pullout loads. *Geotextiles and Geomembranes*, 44(3):230-246. https://doi.org/10.1016/j.geotexmem.2015.11.001

Xiao CZ, Han J, Zhang Z, 2016. Experimental study on performance of geosynthetic-reinforced soil model walls on rigid foundations subjected to static footing loading. *Geotextiles and Geomembranes*, 44(1):81-94. https://doi.org/10.1016/j.geotexmem.2015.06.001

Xu F, Chai JC, 2014. Lateral displacement of PVD-improved deposit under embankment loading. *Geosynthetics International*, 21(5):286-300. https://doi.org/10.1680/gein.14.00016

Yang SC, Leshchinsk B, Zhang F, et al., 2016. Required strength of geosynthetic in reinforced soil structures supporting spread footings in three dimensions. *Computers and Geotechnics*, 78:72-87. https://doi.org/10.1016/j.compgeo.2016.04.010

Yarivand A, Behnia C, Bakhtiyari S, et al., 2017. Performance of geosynthetic reinforced soil bridge abutments with modular block facing under fire scenarios. *Computers and Geotechnics*, 85:28-40. https://doi.org/10.1016/j.compgeo.2016.12.004

Yu Y, Bathurst RJ, 2017. Probabilistic assessment of reinforced soil wall performance using response surface method. *Geosynthetics International*, 24(5):524-542. https://doi.org/10.1680/jgein.17.00019

Yu Y, Bathurst RJ, Allen TM, et al., 2016. Physical and numerical modelling of a geogrid-reinforced incremental concrete panel retaining wall. *Canadian Geotechnical Journal*, 53(12):1883-1901. https://doi.org/10.1139/cgj-2016-0207

Zhou J, Chen JF, Xue JF, et al., 2012. Micro-mechanism of the interaction between sand and geogrid transverse ribs.

Geosynthetics International, 19(6):426-437. https://doi.org/10.1680/gein.12.00028

Zhou M, Liu HL, Chen YM, et al., 2016. First application of cast-in-place concrete large-diameter pipe (PCC) pile-reinforced railway foundation: a field study. *Canadian Geotechnical Journal*, 53(4):708-716. https://doi.org/10.1139/cgj-2014-0547

中文概要

题　目：两种失效模式下传感型土工带在砂土中的变形特性研究

目　的：在加筋土结构中的土工带有拉伸断裂和拔出两种失效模式。研究土工带的变形对预测加筋土结构的潜在滑裂面具有重要意义。为了研究在拉伸断裂和拔出这两种不同失效模式下土工带的变形特征，本文在不同法向压力下对不同长度的传感型土工带开展拉拔试验。

创新点：1. 传感型土工带具有拉敏效应和自检测功能，可以实现土工带在拉伸过程中的应变分布式测量；2. 提出了两种失效模式之间的临界线，该临界线考虑了法向压力和筋材有效长度两个参数，可用于筋材失效模式的初步判断；3. 根据传感型土工带的变形特征，提出了用于初步预判失效模式的预警准则。

方　法：1. 利用传感型土工带的自检测功能，得到拉拔试验过程中筋材应变的分布情况，并进一步分析得到筋材轴向应力和筋材位移的分布情况；2. 根据不同筋材长度和在不同法向压力下的拉拔试验结果，反向拟合得出两种失效模式之间的临界线；3. 通过分析传感型土工带的应变、应力和位移分布结果，总结得出两种失效模式下土工带的变形特征。

结　论：1. 提出的两种失效模式之间的临界线考虑了筋材长度和法向压力两种因素，可对筋材失效模式进行初步判断。2. 根据传感型土工带分布式检测结果和变形特征，建立了用于判断两种失效模式的预警准则；加筋土结构中的筋材在潜在滑裂面处出现应变峰值，且筋材变形从滑裂面处开始向两侧逐步发展；一旦筋材末端应变不再为零，则筋材易被拔出；若筋材末端应变为零，同时滑裂面处筋材应变极值达到断裂伸长率，则筋材易断裂；该准则可用于判断和识别加筋土结构的潜在失效模式。

关键词：土工合成材料；传感型土工带；失效模式；变形特征；拉拔试验